Monte Carlo modeling of optical coherence tomography imaging through turbid media

Qiang Lu, Xiaosong Gan, Min Gu, and Qingming Luo

We combine a Monte Carlo technique with Mie theory to develop a method for simulating optical coherence tomography (OCT) imaging through homogeneous turbid media. In our model the propagating light is represented by a plane wavelet; its line propagation direction and path length in the turbid medium are determined by the Monte Carlo technique, and the process of scattering by small particles is computed according to Mie theory. Incorporated into the model is the numerical phase function obtained with Mie theory. The effect of phase function on simulation is also illustrated. Based on this improved Monte Carlo technique, OCT imaging is directly simulated and phase information is recorded. Speckles, resolution, and coherence gating are discussed. The simulation results show that axial and transversal resolutions decrease as probing depth increases. Adapting a light source with a low coherence improves the resolution. The selection of an appropriate coherence length involves a trade-off between intensity and resolution. © 2004 Optical Society of America

OCIS codes: 170.7050, 170.4500, 290.5850.

1. Introduction

Noninvasive optical imaging methods are of great importance in biological observation and in medical diagnosis *in vivo*. Optical coherence tomography (OCT), which can reveal the subsurface structures of biological tissues, has been studied extensively since its potential was first demonstrated by Huang *et al.*[1] in 1991. Thereafter, in addition to imaging transparent tissue such as eyes,[2] its application has been extended to image high-scattering tissue such as skin.[3] However, when applied to high-scattering tissue, OCT fails to produce the high-quality images obtained with transparent tissue. Multiscattering, which becomes dominant deep under the surface of turbid tissue, degrades image resolution and contrast.[4] In particular, the coherence of scattered light produces speckles, which make the interpretation of OCT images more difficult.[5]

To optimize the OCT technique in biological imaging, much research has been done in the area of theoretical modeling of OCT imaging of turbid media, such as biological tissues: single backscattering,[6] linear system theory,[7] the Monte Carlo method,[4,7–9] the extended Huygens–Fresnel analytical model,[5,10] and so on. Nevertheless, except for the extended Huygens–Fresnel model, none of the available theoretical models of OCT considers the interference of multiscattered light. Incorporated into previous Monte Carlo models[4,8,9] is a coherence gate, which is implemented by comparing the optical path difference between sample and reference arms with the coherence length of the light source.

In this paper we present a new Monte Carlo model for OCT imaging that includes the interference effects of multiscattered light. In our model, named the coherent Monte Carlo (CMC) model, the propagating light is represented by a plane wavelet with its line propagation direction and path length in turbid medium determined by the Monte Carlo technique and with the process of scattering by small particles computed with Mie theory.[11] Because the phase information of light is carried during its line propagation and scattering, the heterodyne signal of OCT is directly simulated. We should point out that the incorporation of phase information into the Monte Carlo technique was first reported by Daria *et al.*[12] to consider the diffraction effects of a focused beam in two-photon microscopy. To study OCT imaging in this paper, we adapt the method of Daria *et al.* by adding Mie theory to calculate the phase variation during scattering.

Q. Lu (luqiang@mail.hust.edu.cn) and Q. Luo are with the Key Laboratory of Biomedical Photonics of the Ministry of Education, Huazhong University of Science and Technology, Wuhan, 430074, China. X. Gan and M. Gu are with the Centre for Micro-Photonics, Swinburne University of Technology, P.O. Box 218, Hawthorn, Victoria 3122, Australia.
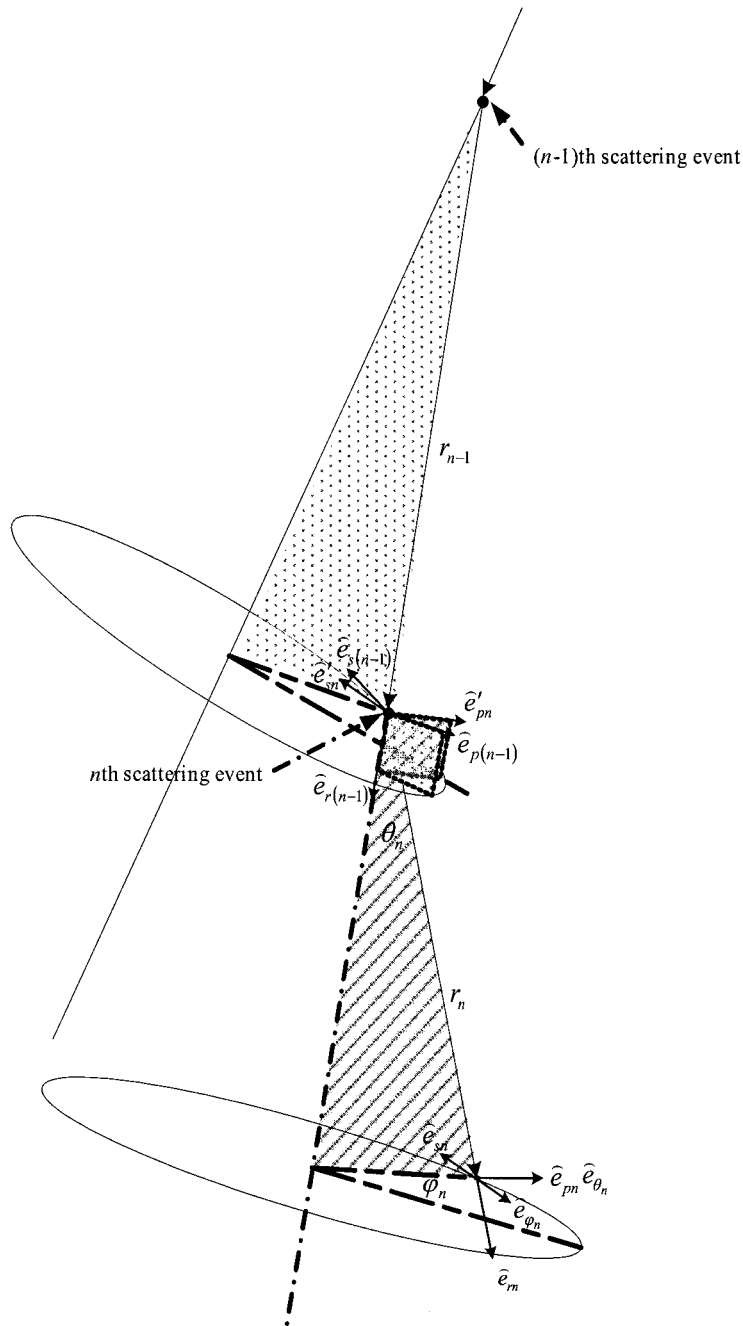
Fig. 1. Geometrical schematic of the transform of the coordinate systems. $\hat{e}$ denotes the unit vector for a given spatial direction. $\hat{e}_{sn}$ and $\hat{e}_{pn}$, $n = 1 \ldots m$ denote unit vectors of perpendicular and parallel components, respectively. r_n, $n = 1 \ldots m$, denotes the free path with length l_n and direction $\hat{e}_{rn}$. θ_n and φ_n, $n = 1 \ldots m$, denote scattering and azimuthal angles, respectively. The relation among these vectors can be denoted by $\hat{e}_s \perp \hat{e}_p$, $\hat{e}_s \times \hat{e}_p = \hat{e}_r$, $\hat{e}_p = \hat{e}_\theta$, $\hat{e}_s = -\hat{e}_\varphi$.

Section 2 describes the basic Monte Carlo technique used to simulate light migration, in which phase information is carried and Jones vectors, instead of intensity, are used to denote light. Also incorporated is a numerical phase function derived from Mie theory. In addition, the model used to simulate polarized OCT imaging through turbid media is illustrated in Section 2. Some results of the simulation are presented in Section 3.

2. Coherent Monte Carlo Techniques

A. Basic Monte Carlo Techniques

We already know that light migration in turbid media is composed of two processes: movement (line propagation) and scattering (see Fig. 1). Therefore the basic Monte Carlo technique used to study light migration includes two random sampling processes: (1) sampling free path length l, which denotes the

moving distance between two adjacent scattering events, and (2) sampling scattering angle θ and azimuthal angle φ, which are used to determine the light propagation direction after scattering. The cross iterations of these two sampling processes, as well as some application-specific constraints, construct the whole simulation process for an individual photon.[13] Calculations of some interesting physical quantities, such as the detected intensity, are performed simply by simulation of a large number of photons and subsequent statistical processing. A detailed description of this process is given below.

To consider coherence in OCT imaging, phase information is included in our CMC model. Jones vectors $\mathbf{E} \equiv (E_p, E_s)^T$, which express both the amplitude and the phase information of two orthogonal electrical field components, parallel component E_p and perpendicular component E_p, are used to identify a wavelet with the help of parameters of position $\mathbf{P} \equiv (x, y, z)^T$ and line propagation direction $\mu \equiv (\mu_x, \mu_y, \mu_z)^T$, which describe a wavelet in global Cartesian coordinates. The superscript T denotes the matrix transpose.

Variation of the Jones vectors of light migration in turbid medium is due to both line propagation and scattering. Following Ref. 12 we treat light as a plane wave during its line propagation. Therefore only the phase, not the magnitude, of the light field is changed during line propagation. In addition, if we disregard the birefringence in the medium, the phase variations of perpendicular and parallel components are equivalent. This variation can be expressed by $T(l_{n-1})$ as follows:

$$\mathbf{E}_n' = T(l_{n-1})\mathbf{E}_{n-1} = \mathbf{E}_{n-1}\exp[j\mathbf{k}l_{n-1}\hat{e}_{r(n-1)}], \quad (1)$$

where $\mathbf{E}_{n-1} \equiv (E_{p(n-1)}, E_{s(n-1)})^T$ denotes light after the $(n-1)$th scattering event, $\mathbf{E}_n' \equiv (E_{pn}', E_{sn}')^T$ denotes light before the nth scattering event, $\mathbf{k}$ is a wave vector in the medium, and l_{n-1} is the free path length. All these quantities are in the coordinate system $(\hat{e}_{s(n-1)}, \hat{e}_{p(n-1)}, \hat{e}_{r(n-1)})$, as shown in Fig. 1. $\hat{e}$ denotes the unit vector.

We know that in scattering of light by an isotropic microsphere, if the incident light is polarized parallel to a scattering plane, then the scattered light is also polarized parallel to the scattering plane. Furthermore, if the incident light is polarized perpendicular to the scattering plane, then the scattered light is also polarized perpendicular to the scattering plane.[11] The nth single scattering event is thus denoted

$$\begin{pmatrix} E_{pn} \\ E_{sn} \end{pmatrix} = S(\theta_n)\begin{pmatrix} E_{pn}'' \\ E_{sn}'' \end{pmatrix}$$
$$= \exp(j\pi/2)\begin{pmatrix} s_2(\theta_n) & \\ & s_1(\theta_n) \end{pmatrix}\begin{pmatrix} E_{pn}'' \\ E_{sn}'' \end{pmatrix}, \quad (2)$$

where $(E_{pn}'', E_{sn}'')^T$ denotes the light field before scattering in the same coordinate system $(\hat{e}_{sn}, \hat{e}_{pn}, \hat{e}_{rn})$ as that of the nth scattered light field $\mathbf{E}_n$, shown in Fig. 1. Scattering matrix $S(\theta_n)$ components $s_1(\theta_n)$ and $s_2(\theta_n)$ are calculated with Mie theory.

Moreover, a project matrix $R(\varphi_n)$ is needed to transform the light field from the coordinate system $(\hat{e}_{s(n-1)}, \hat{e}_{p(n-1)}, \hat{e}_{r(n-1)})$ to $(\hat{e}_{sn}, \hat{e}_{pn}, \hat{e}_{rn})$:

$$\begin{pmatrix} E_{pn}'' \\ E_{sn}'' \end{pmatrix} = R(\varphi_n)\begin{pmatrix} E_{pn}' \\ E_{sn}' \end{pmatrix} = \begin{pmatrix} \cos\varphi_n & -\sin\varphi_n \\ \sin\varphi_n & \cos\varphi_n \end{pmatrix}\begin{pmatrix} E_{pn}' \\ E_{sn}' \end{pmatrix}, \quad (3)$$

where φ_n is the azimuthal angle of the nth scattering event.

Now we can perform matrix vector multiplication and obtain the relation between the Jones vectors of two adjacent scattering events as follows:

$$\begin{pmatrix} E_{pn} \\ E_{sn} \end{pmatrix} = S(\theta_n)R(\varphi_n)T(r_{n-1})\begin{pmatrix} E_{p(n-1)} \\ E_{s(n-1)} \end{pmatrix}. \quad (4)$$

The whole migration process of a single wavelet can thus be expressed as

$$\mathbf{E}_m = T(l_m)S(\theta_m)R(\varphi_m)\ldots T(l_1)S(\theta_1)R(\varphi_1)T(r_0)\mathbf{E}_0. \quad (5)$$

The length $l_n (n = 1 \ldots m)$ is sampled randomly from the exponential distribution $p(l) = 1/l_T\exp(-1/l_T)$, where $l_T = 1/(\mu_s + \mu_a)$ denotes the mean free path (mfp) length and μ_s and μ_a are the scattering coefficient and the absorption coefficient, respectively. The scattering angle θ_n and the azimuthal angle φ_n, $n = 1 \ldots m$, are sampled randomly from the phase function $p(\theta, \varphi)$, which will be discussed in detail in Subsection 2.B.

In Monte Carlo simulation a large number of independent wavelets are launched. The light field is the superposition of all possible contributions from Eq. (5), which yields

$$\mathbf{E}_{\text{mean}} = \sum_{i=1}^{N}\mathbf{E}_{i,m}$$
$$= \sum_{i=1}^{N}\left\{ M\prod_{n=1}^{m}[T(l_{i,n})S(\theta_{i,n})R(\varphi_{i,n})]T(l_0)\mathbf{E}_{i,0}\right\}, \quad (6)$$

where i denotes the sum over all detected wavelets and n denotes multiplication over all scattering events of a single wavelet. The translation of the light field from the local coordinate system to the global one is considered via matrix M, which satisfies following equation:

$$(\hat{e}_{sm}, \hat{e}_{pm}, \hat{e}_{rm}) = (\hat{e}_x, \hat{e}_y, \hat{e}_z)M,$$

where $(\hat{e}_x, \hat{e}_y, \hat{e}_z)$ denotes unit vectors of the global Cartesian coordinate system and $(\hat{e}_{sm}, \hat{e}_{pm}, \hat{e}_{rm})$ denotes the local coordinate system of the wavelet's final scattering event.

Considering $\prod_{n=0}^{m}T(l_n)$ can be translated to $\exp(j\mathbf{k}\sum_{n=0}^{m}l_n)$, in a practical simulation the variation of the Jones vectors brought by line propagation is calculated separately by addition, instead of multiplication, to improve the calculation efficiency. Other details, such as position and direction transforms, are the same as those of the conventional Monte Carlo
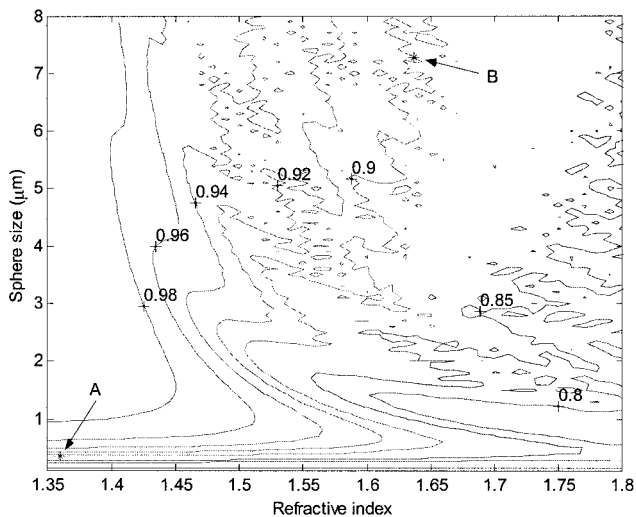
Fig. 2. Contours of g values for microspheres with different radii and different refractive indices. The refractive index of the medium is 1.33; wavelength, 0.6328 μm. The g value is 0.9 in point A (1.3603, 0.3577) and in point B (1.6303, 7.2737).

Fig. 3. Mie and H–G phase functions with the same g value of 0.9 for points A and B, which correspond to those in Fig. 2.

technique, which is illustrated in detail in Refs. 13 and 14.

B. Mie Theory and Numerical Mie Phase Function

To control the optical properties conveniently, a turbid suspension (phantom) consisting of aqueous polystyrene microspheres, instead of a biological sample, is usually used in tissue optics research. Mie theory provides an exact solution of a plane wave scattered by an isotropic microsphere.[11] Therefore the optical properties, such as the scattering coefficient μ_s, the absorption coefficient μ_a, and the anisotropic factor g, of the phantom can be directly calculated with Mie theory instead of being experimentally measured. In the CMC model, scattering matrix components $s_1(\theta_n)$ and $s_2(\theta_n)$ in Eq. (2) are also calculated with Mie theory.

Furthermore, in our CMC model, the phase function $p(\theta, \varphi)$ is also obtained with Mie theory. As we know, the Henyey–Greenstein (H–G) phase function was widely adopted in previous Monte Carlo simulations[13,14] to sample the scattering angle θ, and the uniform distribution from 0 to 2π was adopted to sample the azimuthal angle φ. The H–G phase function, determined only by the anisotropic factor g, was considered as a good approximation of Mie theory results.[14]

However, here we illustrate why the H–G phase function is not good enough. First, its single-parameter anisotropic factor g is not sufficient to reflect the angular distribution of scattered light, which is determined by the microsphere size relative to the wavelength and the refractive index of the microsphere relative to that of the solution. In biological tissue scatter size ranges from 0.2 μm (peroxisome) to 10 μm (nucleus), and refractive indices range from 1.38 to 1.7.[15] Using these ranges, we present the g-value contours in Fig. 2. The solution is calculated
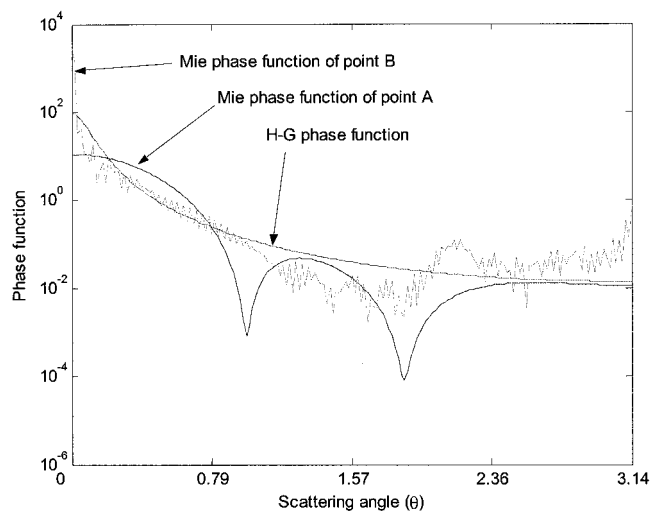
with a refractive index of 1.33 and a wavelength of 0.6328 μm. From this figure we conclude that the phase function could be described exactly only with two parameters. We take two points A (1.3603, 0.3577) and B (1.6303, 7.2737) from this figure, in which both g values equal 0.9, and plot their phase functions in Fig. 3, along with the corresponding H–G phase function ($g = 0.9$). From Fig. 3 it is clear that, for large microspheres (point B, radius 7.2737 μm), the H–G phase function underestimates the intensity of light scattered at small angles in the forward and backward directions. However, for small microspheres (point A, radius 0.3577 μm), the H–G phase function overestimates the intensity of light scattered at small and intermediate angles in the forward direction.

Second, if polarized incident light is considered, the supposedly uniform distribution used to sample the azimuthal angle φ is also not cogent enough. We calculated the two-dimensional intensity distribution of light scattered over a 4π solid angle Ω when a linearly polarized plane wave is incident. As we know, the angle between the polarization plane of incident light and the scattering plane is the azimuthal angle φ. The result is shown in Fig. 4, in which it is clear that that distribution over φ is not uniform. In addition, the distribution of the intensity over φ is different for different scattering angles θ.

Given the above discussion, our CMC model uses a two-dimensional phase function $p(\theta, \varphi)$, which is equivalent to that used in Ref. 4:

$$
\begin{aligned}
p(\theta, \varphi) \propto I_s(\theta, \varphi) = {}& \cos^2 \varphi [|s_2(\theta) E_p|^2 + |s_1(\theta) E_s|^2] \\
& + \sin^2 \varphi [|s_2(\theta) E_s|^2 + |s_1(\theta) E_p|^2] \\
& - \sin 2\varphi [|s_2(\theta)|^2 \\
& - |s_1(\theta)|^2] \mathrm{Re}(E_p E_s^*), \quad (7)
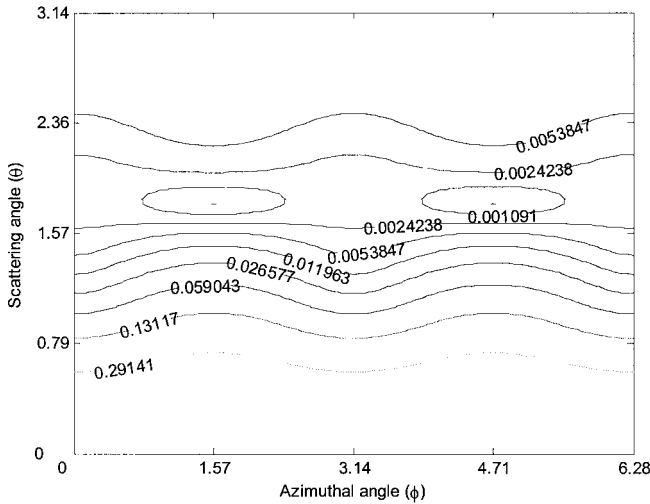\end{aligned}
$$

Fig. 4. Contours of the calculated two-dimensional phase function $p(\theta, \phi)$ with a microsphere refractive index of 1.55, medium refractive index of 1.33, microsphere radius of 0.2 μm, and wavelength of 0.6328 μm.

where $p(\theta, \phi)$ is normalized by $\int_{4\pi} p(\theta, \varphi)d\Omega = 1$ and $I_s(\theta, \varphi)$ denotes the intensity of scattered light.

In this paper superscript * denotes the conjugate. From Eq. (7) we know that, in the case of polarized light, the incidence phase function depends not only on the properties of the turbid medium, such as microsphere size, microsphere refractive index, and solution refractive index, but also on light properties such as wavelength and polarization status.

In practical coding θ and φ are sampled with a method of conditional possibility, $p(\theta, \varphi) = p_{\varphi|\theta}(\varphi)p_\theta(\theta)$. θ is sampled according to $p_\theta(\theta)$ as follows:

$$p_\theta(\theta) = \int_{2\pi} p(\theta, \varphi)d\varphi$$
$$= [|s_1(\theta)|^2 + |s_2(\theta)|^2](|E_p|^2 + |E_s|^2)$$
$$= [|s_1(\theta)|^2 + |s_2(\theta)|^2]I_i, \qquad (8)$$

where I_i denotes incident light intensity. Equation (8) shows that $p_\theta(\theta)$ is independent of the polarization status of incident light, which means that $p_\theta(\theta)$ could be precalculated numerically before the wavelet random walk to save computational resources. The scattering matrix components s_1 and s_2 are determined based on the sampled value of the scattering angle θ_n. Subsequently, with the known light field components E_p and E_s the azimuthal angle φ is numerically sampled according to $p_{\varphi|\theta_n}(\varphi)$:

$$p_{\varphi|\theta_n}(\varphi) = A \cos^2 \varphi + B \sin^2 \varphi + C \sin 2\varphi, \qquad (9)$$

where

$$A \equiv |s_2(\theta_n)E_p|^2 + |s_1(\theta_n)E_s|^2,$$
$$B \equiv |s_2(\theta_n)E_s|^2 + |s_1(\theta_n)E_p|^2,$$
$$C \equiv [|s_1(\theta_n)|^2 - |s_2(\theta_n)|^2]\mathrm{Re}(E_pE_s^*).$$

In conclusion, in the same Monte Carlo process, the distribution of the scattering angle θ [Eq. (8)] is calculated only once and is used repetitiously to sample θ in every scattering event, whereas the distribution over azimuthal angle φ [Eq. (9)] should be calculated for every scattering event and thereafter used to sample φ.

C. Model of Optical Coherence Tomography Imaging through Turbid Media

An OCT system is an extension of a Michelson interferometer, which incorporates a low-coherence light source instead of a high-coherence laser source.[1] The light reflected from the sample arm interferes with the light from the reference arm only if the difference between their optical path lengths is within the coherence length of the light source. The detected heterodyne signal could be expressed as[16]

$$I^{\mathrm{het}} = \mathrm{Re}\left\{ (E^R)^* \sum_n E_n{}^s(t)\Gamma[L_n(t)] \right\}, \qquad (10)$$

where E^R denotes the light reflected from the reference arm and $E_n{}^s$ denotes the light reflected from the sample arm along a different path n. $\Gamma[L_n(t)]$ is the low-coherence function, and $L_n(t)$ is the overall path-length difference of the nth wavelet with the reference arm.

Moreover, the low-coherence function is simulated with the following principle[8]:

$$\Gamma(L_n) = 1, \qquad \text{if } |L_n| < L_c/2$$
$$= 0, \qquad \text{else,} \qquad (11)$$

where L_c is the coherence length. If a wavelet satisfies $\Gamma(L_n) = 1$, it is detected and recorded as a signal. Otherwise, it is discarded. Equation (11) implies that the coherence function in the simulation is a non-Gaussian square function in reality. Also, in our CMC model the reference light field E^R is set to 1 to simplify the simulation.

To simulate OCT imaging through turbid media, a full-reflect mirror with a sharp edge is embedded in a turbid phantom. By varying the length of the reference arm, axial scanning is implemented, and the axial image is obtained. In the CMC model the interfered signal is demodulated by use of the Hilbert transform[17] and a low-pass filter. The low-pass filter is designed as a ninth-order Butterworth low-pass filter with a stop band equal to the sampling spatial frequency $1/0.09$ μm $\times 0.015$.

3. Results and Discussion

A. Validation

A computational case for studying the polarization status of diffusely scattered light is used to validate the CMC program. The simulated experiment is the same as that in Ref. 18. One element of the Mueller matrix m_{12} for suspensions of 0.204-μm-diameter microspheres is calculated. To achieve the same conditions used in the standard Monte Carlo method, the
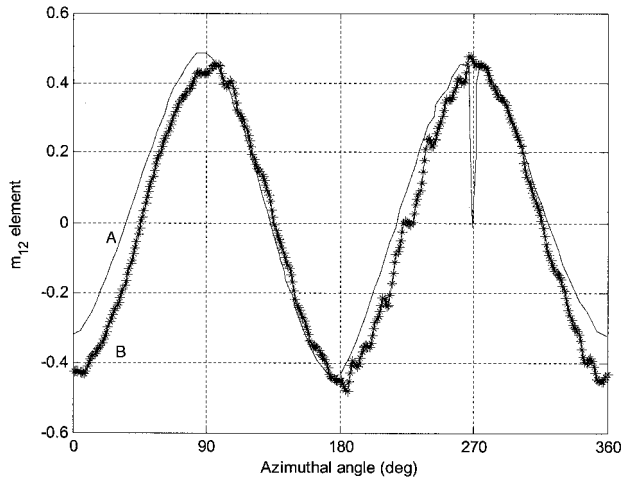
Fig. 5. Comparison of our CMC program with that reported in Ref. 18. Plot A is the m_{12} value from Ref. 18, and plot B is that from our CMC program.

Fig. 6. Intensities of transmitted light for different phase functions. Points A and B have the same g value of 0.9 and correspond to those in Fig. 2. Number densities of microspheres in the solution are selected to equal the mfp value of 100 μm. The turbid phantom has a thickness of 300 μm.

interference between different wavelets is not considered, which means that the components of the Stokes vectors $(I, Q, U, V)^T$ are calculated by use of the statistical expression of $I = \Sigma_n |E_n|^2$, not $I = |\Sigma_n E_n|^2$. The element m_{12} is simulated by calculating the total reflected intensity for linearly x-polarized incident light and subtracting from this the total reflected intensity for linearly y-polarized incident light.[19] The values of the m_{12} element on a ring with a 1-cm radius centered on a light-incident point are shown in Fig. 5 and serve to validate the CMC program to some extent.

B. Effects of Phase Function

A simulation case of the transmitted intensity of a linearly polarized light perpendicularly incident on the surface is made in support of our discussion of phase function presented in Subsection 2.B. The distributions of the transmitted intensity over the radial distance are given in Fig. 6, from which it is apparent that, at small angles in the forward direction, the H–G phase function underestimates the intensity for phantoms with large microspheres (point B) and overestimates that for phantoms with small microspheres (point A).

In Fig. 7 the spatial distributions of the degrees of polarization (DOP) are given. DOP is defined as

$$\text{DOP} = (Q^2 + U^2 + V^2)^{1/2}/I. \qquad (12)$$

The parameters used in the simulations are the same as those shown in Fig. 6. The x-polarized light is incident. First, comparing Figs. 7(a) with 7(b) and Figs. 7(c) with 7(d), we find that the H–G phase function lacks the ability to reflect the spatial distributions of the DOP exactly. The notable difference between the DOPs in the x direction (horizontal) and the y direction (vertical) is not apparent from the results for the H–G phase function. Second, we notice that, if we adapt the numerical Mie phase function, such as in Figs. 7(a) and 7(c), the effect of
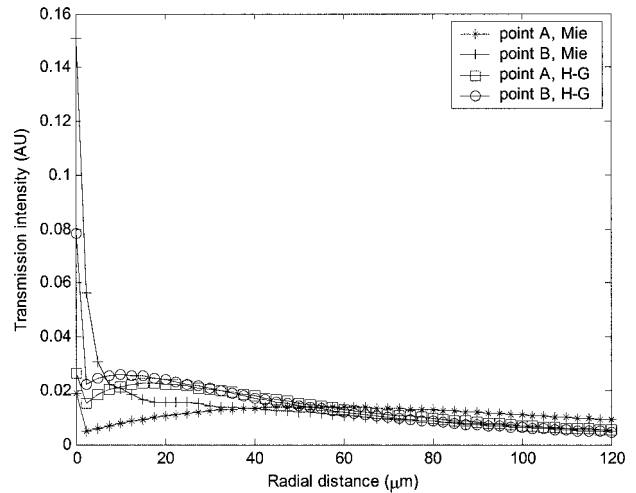
microsphere size on polarization is obvious; however, this effect is not apparent from a similar comparison of Figs. 7(b) with 7(d).

C. Optical Coherence Tomography Axial Image

To study the effect of OCT probing depth on signal attenuation, a sharp-edged mirror is embedded in an aqueous suspension of polystyrene microspheres at different depths under the surface. The preparation is of indefinite size in transversal dimensions. The incident infinitely narrow light is x polarized and is incident perpendicular to the surface of the sample.
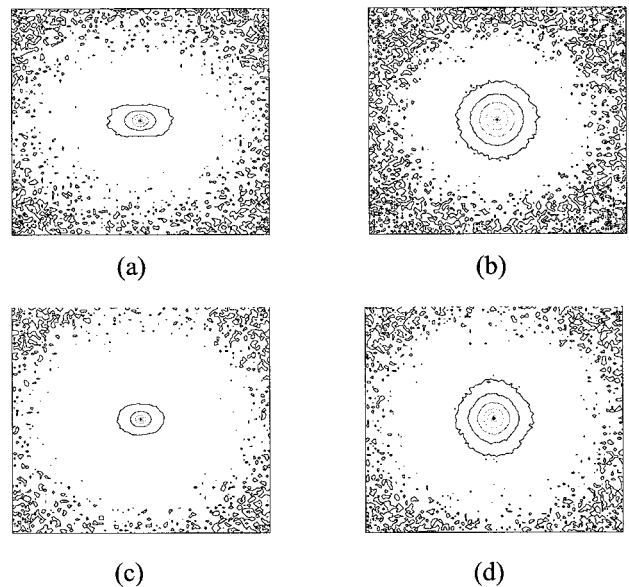

(a)

(b)

(c)

(d)

Fig. 7. Patterns of the DOP for different phase functions: (a) point A with Mie phase function, (b) point A with H–G phase function, (c) point B with Mie phase function, (d) point B with H–G phase function. Pattern size is 1 mm × 1 mm.
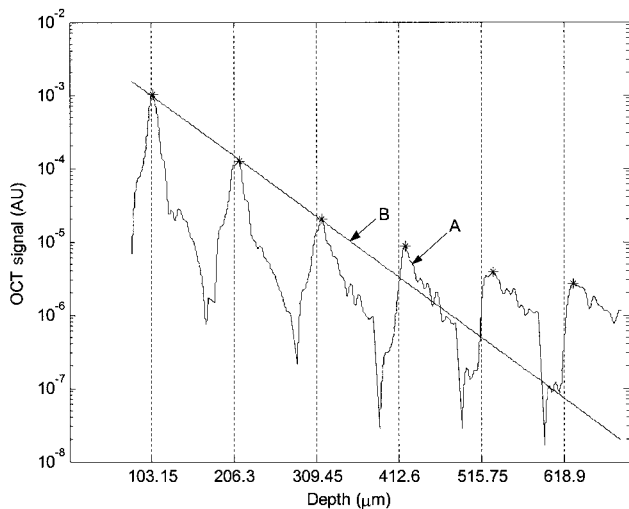
Fig. 8. Simulated one-dimensional axial image with the following parameters: microsphere of size 1.2 μm and refractive index of 1.565 in an aqueous suspension (refractive index 1.329) with a number density of 0.006 per cubic micrometer. The sharp-edged mirror is embedded at a depth of 1–6 mfp's under the surface (1 mfp = 103.15 μm). The wavelength is 0.8 μm. Plot A is the simulated OCT signal, and plot B is the exponential fit curve of data at 1–3 mfp's. The coherence length of the light source is 7.5 μm in free space. The detector has a radius of 100 μm.
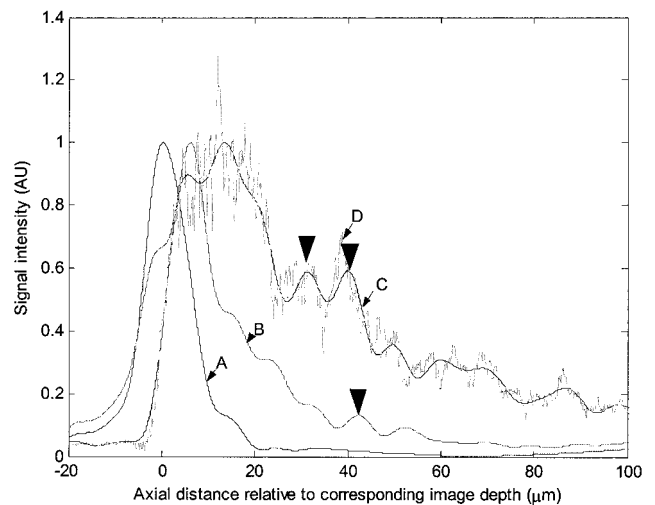

Fig. 9. Axial images of a sharp-edged mirror embedded at different depths. The parameters are the same as those in Fig. 8. Plots A, B, and C denote the images at depths of 1, 3, and 5 mfp's, respectively. Plot D is the image without a low-pass filter. Plot C is the envelope of the raw image demodulated after the Hilbert transform.

The embedded sharp edge also lies in the x direction. With 10^8 wavelets simulated for each Monte Carlo, the OCT axial images of this kind of phantom are obtained. For every depth category, five images are obtained and are averaged to suppress speckles.[20] All of the simulation results are shown in Fig. 8, in which each peak represents an image of the sharp-edged mirror at a given depth. From Fig. 8, three observations may be made. First, we observe that the signal intensity decreases with increasing depth. The signal attenuation rate approximates the exponential reduction function (plot B, solid line) at shallow depths. As the depth increases further, the signal attenuation rate slows down. We infer that this phenomenon arises because least scattering is dominant at shallow depths, whereas multiscattering is dominant at great depths. This so-called shower curtain effect (see Ref. 9) is important for calculating the OCT signal at deep depths. Apparently, if we omit this effect, as did the analysis in Ref. 6, the OCT signal at great depths is underestimated by several orders of magnitude. Second, we find that the axial positions of the image deviate from the setting positions of object (sharp-edged mirror). Moreover, the extent of the deviation increases with increasing depth. We infer that this effect is also caused by multiscattering in turbid media. This effect should be considered in spatial measurements of turbid samples by the adaptation of the OCT technique or by the restoration of the OCT image. Gan *et al*.[21] reported a similar phenomenon in their study of single- and two-photon microscopy. However, to our knowledge, the present study is the first one to consider the axial deviate effect of the OCT image. Finally, it is

observed that the peak width, which reflects the axial resolution, roughly increases as the depth increases, implying that the axial resolution is reduced as the probing depth increases.

D. Optical Coherence Tomography Speckles

To clearly illustrate the effect of multiscattering on the image, we present in Fig. 9 images in which the object is embedded at different depths, all of which are normalized to the maximal value. The transverse axis is the axial distance relative to a given sharp-edged mirror depth. Comparing plots A, B, and C in Fig. 9, we observe more clearly the two effects also seen in Fig. 8. First, the peak is broadened by multiscattering with increasing depth. Second, the deviation effect is illustrated more clearly. Moreover, in Fig. 9, particularly in plot C, we observe many small peaks, some of which are marked by inverse triangles. These peaks are several micrometers ($\gg\lambda$) in size and represent speckles encountered in OCT imaging of turbid media.[20] If we consider a raw image without Butterworth filtering (plot D), the speckles are clearer and more numerous and include many high-frequency spikes of size $\sim\lambda$. Considering their different frequencies, these speckles are classified into two categories: interferogram speckle of size $\gg\lambda$ and phase fluctuation speckle of size $\sim\lambda$. The interferogram speckle is comparable in size with the minimal resolvable structure and thus complicates the interpretation of the OCT image. In our simulation we found that the number and relative magnitude of interferogram speckles increase as the probing depth increases. On the other hand, the level of phase fluctuation speckles remains fairly constant across different probing depths, a trend that is not shown in this figure. We know that speckles are
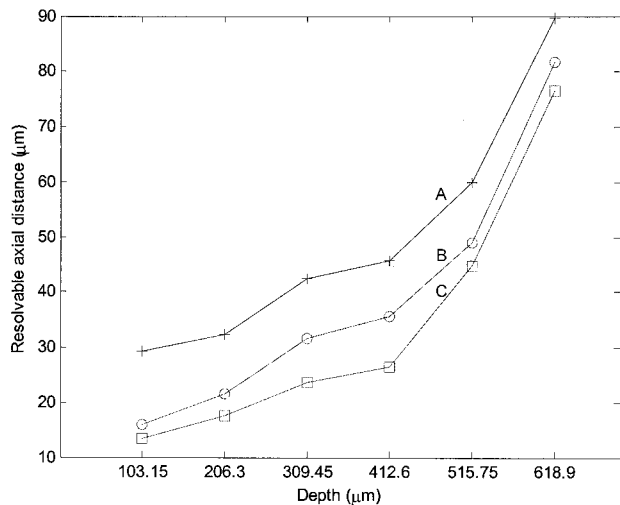
Fig. 10. Axial resolution as a function of the depth at which a sharp-edged mirror is embedded. Results with coherence lengths of 30 μm (plot A), 15 μm (plot B), and 7.5 μm (plot C) are presented.
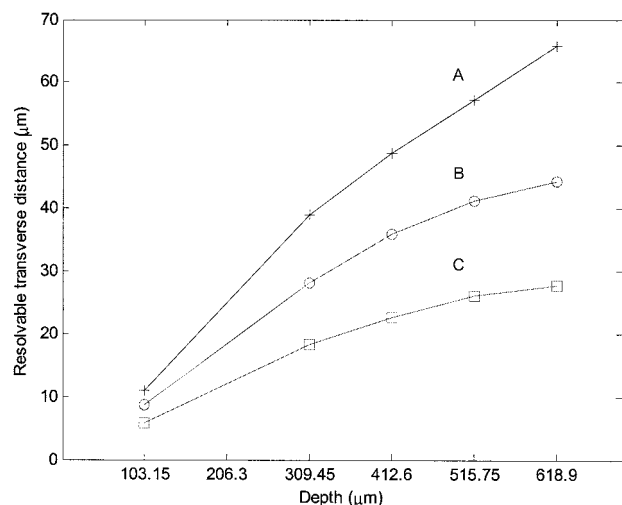

Fig. 11. Transverse resolution as a function of the depth at which a sharp-edged mirror is embedded. Results with coherence lengths of 30 μm (plot A), 15 μm (plot B), and 7.5 μm (plot C) are presented.

caused by interference between beams of light with different phases. Light transported in turbid media has a phase variation that is composed of two parts: line propagation and scattering. We deduce that the phase variation from line propagation contributes mainly to interferogram speckles, whereas that from scattering contributes mainly to phase fluctuation speckles. Given the different characteristics and different sources of these speckle types, we know that digital filters, such as the wavelet filter,[22] are very effective at suppressing high-frequency phase fluctuation speckles, but have a limited capability in removing interferogram speckles. Besides, the method of averaging uncorrelated speckle patterns (i.e., images are taken at different angles of incidence and are then averaged; see Ref. 23) performs well in suppressing interferogram speckles.

E. Optical Coherence Tomography Resolutions

In Fig. 10 the dependence of axial resolution on imaging depth is illustrated. Axial resolution is denoted by the axial resolvable distance, which is defined as the width of the image of a sharp-edged mirror at a magnitude relative to the maximum value equal to e^{-1}. A larger resolvable distance denotes a lower resolution. From Fig. 10 we first observe that axial resolution decreases as probing depth increases. Moreover, the deeper the depth the faster this change occurs. Second, comparisons of plots A, B, and C show that longer coherence lengths yield lower axial resolutions. Usually, the OCT axial resolution is considered to be the coherence length of the light source. However, given the above simulation result, it is shown that, when OCT is used to image turbid media such as a biological sample, the coherence length as the resolution limit cannot always be reached. Multiscattering of a turbid sample blurs the image and thus reduces the resolution to a large extent.

Transverse resolution is denoted by the transverse resolvable distance, which is defined as the width of sharp-edged mirror image at 10% and 90% intensity that has been normalized to the maximum value.[24] To facilitate the simulation of transverse scanning, we introduced the effective point-spread function in our Monte Carlo simulation. Similar to that reported in Ref. 24, the effective point-spread function used here for OCT is defined by the distribution of photons that can propagate through a turbid medium and reach a detector in the imaging region. According to this technique, only the interference between light from the reference arm and the sampling arm is considered, and the interference among the different sampling paths is omitted. The transverse resolution of OCT is generally known to be dependent on the waist radius of the focused Gaussian incident beam. However, the light source in our simulation is of infinite size, which means that no focusing effect is considered. Under this condition, the dependence of the transverse resolution of OCT on imaging depth for different coherence lengths is given in Fig. 11, from which it is shown that greater probing depths yield lower transverse resolutions. Additionally, longer coherence lengths yield lower transverse resolutions. Comparing the results from Figs. 10 and 11, we find that, with increasing depth, the axial resolution drops faster than the transverse resolution does. This implies that the loss of axial resolution might be the factor limiting the OCT's penetration depth.

F. Coherence Gating

In Fig. 12 the dependence of the axial resolution on the coherence length for different probing depths is given. From Fig. 12 it is shown that a longer coherence length yields a lower axial resolution when probing depth is given. This implies that adapting the
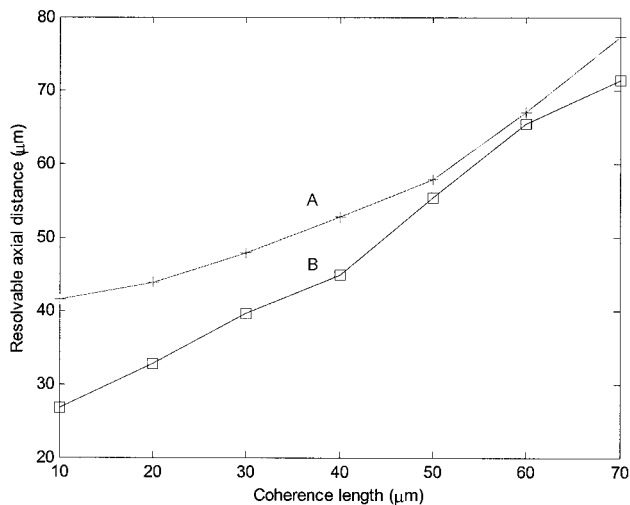
Fig. 12. Axial resolution as a function of coherence length for different image depths. Light with wavelength of 0.6328 μm incidents on the turbid medium, which is composed of microspheres with a radius of 1.0 μm, a refractive index of 1.573, and a number density of 0.006 per cubic micrometers suspended in water, which has a refractive index of 1.332. Results for image depths of 5 mfp (plot A; 1 mfp = 155 μm) and 3 mfp (plot B) are given.

light source with a low coherence length can improve axial sectioning ability. The effect of coherence length on signal intensity is shown in Fig. 13, in which we observe that a lower coherence length yields a lower signal intensity. From these two observations, we conclude that the coherence length of a light source plays a gating role in OCT imaging. The selection of the coherence length is a trade-off between the resolution and the intensity. However, from Fig. 13 we know that, at large sizes (e.g., larger than 30 μm in plot A), the coherence length affects signal intensity only mildly. This phenomenon implies that relatively high resolution could be obtained
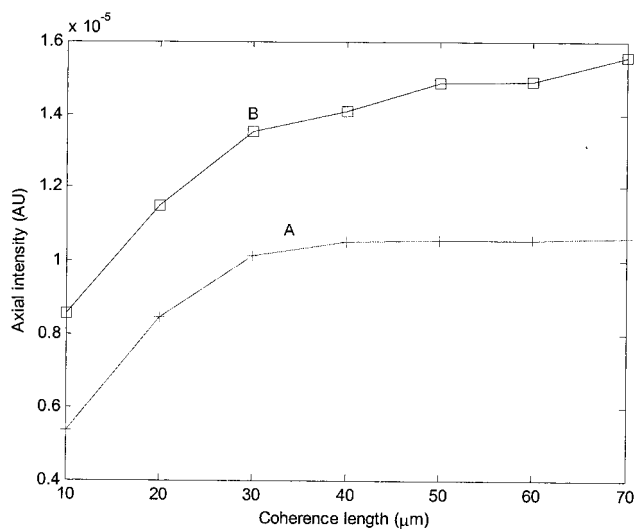

Fig. 13. Signal intensity as a function of coherence length for different image depths. The parameters are the same as those used in Fig. 12.

while preserving sufficient signal intensity. In addition, by comparing results from cases with different probing depths we find that the effect of coherence gating increases with increasing probing depth.

4. Conclusions

In this paper we report a novel Monte Carlo model (CMC) that incorporates Mie theory to calculate the effect of small-particle scattering on a light field. Compared with the standard Monte Carlo method (see Ref. 14), which adapts only intensity to denote photons and thus does not include wave properties, CMC, which adapts Jones vectors to denote light and thus considers magnitude and phase information, brings the capability of simulating the interference between multiscattered light. This improvement has great potential for studying other kinds of coherence imaging techniques in biomedical optics. In addition, incorporated in the CMC model is a two-dimensional numerical phase function, which is obtained from Mie theory. A comparison of the numerical phase function with the conventional H–G phase function shows the superior performance of the former.

The CMC model is applied to simulate OCT imaging of an object under the surface of a turbid sample. In this context, speckles, resolution, and coherence gating are discussed. The simulation results ascribe speckles to two sources: line propagation and scattering. The simulations also reveal that, when used to image an object under the surface of a turbid sample, OCT's axial and transversal resolutions cannot reach their corresponding theoretical limits: coherence length and diffractive limit, respectively. Resolution decreases as probing depth increases. However, adapting the light source with a lower coherence can improve the resolution. Furthermore, the selection of a light source with an appropriate coherence length involves a trade-off between intensity and resolution.

References

1. D. Huang, E. A. Swanson, C. P. Lin, J. S. Schuman, W. G. Stinson, W. Chang, M. R. Hee, T. Flotte, K. Gregory, C. A. Puliafito, and J. G. Fujimoto, "Optical coherence tomography," Science **254,** 1178–1181 (1991).
2. C. A. Puliafito, M. R. Hee, C. P. Lin, E. Reichel, J. S. Schuman, J. S. Duker, J. A. Izatt, E. A. Swanson, and J. G. Fujimoto, "Imaging of macular disease with optical coherence tomography," Opthalmology **120,** 217–229 (1995).
3. J. M. Schmit, M. Yadlowsky, and R. F. Bonner, "Subsurface imaging of living skin with optical coherence microscopy," Dermatology **191,** 93–98 (1995).
4. G. Yao and L. V. Wang, "Monte Carlo simulation of an optical coherence tomography signal in homogeneous turbid media," Phys. Med. Biol. **44,** 2307–2320 (1999).
5. J. M. Schmitt and A. Knuttel, "Model of optical coherence tomography of heterogeneous tissue," J. Opt. Soc. Am. A **14,** 1231–1242 (1997).

6. J. A. Izatt, M. R. Hee, G. M. Owen, E. A. Swanson, and J. G. Fujimoto, "Optical coherence microscopy in scattering media," Opt. Lett. **19,** 590–592 (1994).

7. Y. Pan, R. Birngruber, J. Rosperich, and R. Engelhardt, "Low-coherence optical tomography in turbid tissue: theoretical analysis," Appl. Opt. **34,** 6564–6574 (1995).

8. D. J. Smithies, T. Lindmo, Z. P. Chen, J. S. Nelson, and T. E. Milner, "Signal attenuation and localization in optical coherence tomography studied by Monte Carlo simulation," Phys. Med. Biol. **43,** 3025–3044 (1998).

9. A. Tycho, T. M. Jorgensen, H. T. Yura, and P. E. Anderson, "Derivation of a Monte Carlo method for modeling heterodyne detection in optical coherence tomography systems," Appl. Opt. **41,** 6676–6691 (2002).

10. L. Thrane, H. T. Yura, and P. E. Andersen, "Analysis of optical coherence tomography systems based on the extended Huygens–Fresnel principle," J. Opt. Soc. Am. A **17,** 484–490 (2000).

11. C. F. Bohren and D. R. Huffman, *Absorption and Scattering of Light by Small Particles* (Wiley, New York, 1983).

12. V. R. Daria, C. Saloma, and S. Kawata, "Excitation with a focused, pulsed optical beam in scattering media: diffraction effects," Appl. Opt. **39,** 5244–5255 (2000).

13. I. Lux and L. Koblinger, *Monte Carlo Particle Transport Methods: Neutron and Photon Calculations* (CRC Press, Boca Raton, Fla., 1991).

14. L. H. Wang, S. L. Jacques, and L. Q. Zheng, "MCML-Monte Carlo modeling of photon transport in multi-layered tissues," Comput. Methods Programs Biomed. **47,** 131–146 (1995).

15. A. Dunn, "Light scattering properties of cells," Ph.D. dissertation (University of Texas at Austin, 1997).

16. A. L. Petoukhova, W. Steenbergen, and F. F. M. De Mul, "Path-length distribution and path-length-resolved Doppler measurements of multiply scattered photons by use of low-coherence interferometry," Opt. Lett. **26,** 1492–1494 (2001).

17. Y. Zhao, Z. Chen, Z. Ding, H. Ren, and J. S. Nelson, "Real-time phase resolved functional optical coherence tomography by use of optical Hilbert transformation," Opt. Lett. **27,** 98–100 (2002).

18. S. Bartel and A. H. Hielscher, "Monte Carlo simulations of the diffuse backscattering Mueller matrix for highly scattering media," Appl. Opt. **39,** 1580–1588 (2000).

19. A. H. Hielscher, A. A. Eick, J. R. Mourant, D. Shen, J. P. Freyer, and I. J. Bigio, "Diffuse backscattering Mueller matrices of highly scattering media," Opt. Express **1,** 441–543 (1997), http://www.opticsexpress.org.

20. J. M. Schmitt, "Array detection for speckle reduction in optical coherence microscopy," Phys. Med. Biol. **42,** 1427–1439 (1997).

21. X. Gan and M. Gu, "Spatial distribution of single-photon and two-photon fluorescence light in scattering media: Monte Carlo simulation," Appl. Opt. **39,** 1575–1579 (2000).

22. S. H. Xiang, L. Zhou, and J. M. Schmitt, "Speckle noise reduction for optical coherence tomography," in *Optical and Imaging Techniques for Biomonitoring III*, H.-J. Foth, R. Marchesini, and H. Podbielska, eds., Proc. SPIE **3196,** 79–88 (1998).

23. M. Bashkansky and J. Reintjes, "Statistics and reduction of speckle in optical coherence tomography," Opt. Lett. **25,** 545–547 (2000).

24. X. Gan, S. Schilders, and M. Gu, "Fluorescence microscopic imaging through tissue-like turbid media," J. Appl. Phys. **87,** 3214–3221 (2000).